Aptamer-enhanced immunotherapy targeting Non-Small Cell Lung Cancer cells: A conceptual approach towards T-cell mediated therapy

Priyatharcini Kejamurthy
SRM Institute of Science and Technology
Yash Sansare
SRM Institute of Science and Technology
K. T. Ramya Devi
ramyakanth3@gmail.com

SRM Institute of Science and Technology

Research Article

Keywords: PD-L1 aptamer, Aptamer63, Non-small-cell lung cancer (NSCLC), Immune checkpoint inhibition, Cancer immunotherapy

Posted Date: January 6th, 2026

DOI: https://doi.org/10.21203/rs.3.rs-8243965/v1

Additional Declarations: No competing interests reported.

Abstract

Despite clinical advances with immune checkpoint inhibitors targeting the PD-1/PD-L1 axis, therapeutic response remains limited, as nearly 60% of PD-L1–positive patients fail to benefit from anti-PD-L1 monoclonal antibody therapy. Aptamers are short, single-stranded DNA or RNA oligonucleotides that selectively bind to target molecules with high affinity and specificity. Compared to monoclonal antibodies, aptamers offer several advantages, including lower production cost, faster synthesis, improved thermal stability, longer shelf life, and minimal immunogenicity, making them attractive candidates for targeted cancer therapy. In this study, we designed DNA aptamers specific to the immune checkpoint receptor PD-L1, which is overexpressed on non-small cell lung cancer (NSCLC) cells and serves as a key regulator of tumour-induced immune suppression. Using comprehensive in silico screening, structural modelling, and interaction analysis, aptamer63 was identified as the strongest PD-L1 binder based on predicted thermodynamic stability and molecular interaction energy profiles.

To experimentally validate its functional potential, aptamer63 was fluorescently labelled with TAMRA and visualised under a fluorescence microscope, confirming its binding to the cell surface of PD-L1–expressing NCI-H460 NSCLC cells. Subsequent in vitro assays assessed the immunomodulatory effect of aptamer63 in the presence of activated T lymphocytes. MTT and trypan blue dye exclusion assays demonstrated a dose-dependent reduction in tumour cell viability, with significant inhibition observed at 100nM and 200nM. Hoechst 33342/propidium iodide dual staining confirmed increased apoptotic cell populations, showing the highest apoptosis rate at 100nM. Flow cytometry further revealed a marked decrease in viable cell count across all tested concentrations, with the greatest reduction again observed at 100nM.

Collectively, these results indicate that aptamer63 enhances T cell–mediated cytotoxicity against NSCLC cells, with maximum antitumour efficacy at 100nM.

Overall, these findings establish aptamer63 as a promising PD-L1-blocking immunotherapeutic candidate for NSCLC and demonstrate a rational design pipeline for developing next-generation aptamer-based immune checkpoint inhibitors.

1. Introduction

Cancer remains a critical global health challenge. According to the latest estimates from the International Agency for Research on Cancer (IARC), in 2022, there were approximately 20 million new cancer cases diagnosed worldwide, resulting in 9.7 million deaths. Among all malignancies, lung cancer stands as the leading cause of cancer-related mortality globally, accounting for 2.5 million new cases (12.4% of all cancers) and 1.8 million deaths (18.7% of all cancer deaths) in 2022, making it the most commonly occurring cancer worldwide. While smoking remains the predominant risk factor, non-smokers also develop lung cancer due to second-hand smoke exposure, occupational hazards, air pollution, and genetic predisposition, highlighting the disease's multifactorial aetiology and the need for comprehensive research, prevention strategies, and diverse therapeutic approaches. The projections

indicate that lung cancer burden will continue to increase, with over 35 million new cancer cases predicted by 2050, representing a 77% increase from 2022 estimates (*Global Cancer Burden Growing, amidst Mounting Need for Services)*.

Contemporary cancer treatment encompasses surgical resection, chemotherapy, radiation therapy, targeted therapies, and immunotherapy, each aiming to eliminate malignant cells while minimizing damage to healthy tissues. In recent years, two significant advances have transformed the oncology landscape: the emergence of immuno-oncology and the targeting of actionable oncogenic alterations in genetically driven tumours. However, substantial challenges persist, including tumour heterogeneity, acquired resistance mechanisms, clinical interpretation of complex genomic data, and limited response rates to current therapies. Immune checkpoint inhibitors, particularly monoclonal antibodies targeting cytotoxic T lymphocyte antigen-4 (CTLA-4) and the programmed death-1/programmed death-ligand 1 (PD-1/PD-L1) axis, have demonstrated survival benefits but are effective in only a limited subset of patients. Specifically, studies indicate that approximately 60% of patients with PD-L1-expressing tumours fail to respond to anti-PD-L1 monoclonal antibody therapy, underscoring the need for therapeutic alternatives (Ai et al., 2024; Lim et al., 2020).

Immunotherapy has emerged as a particularly important treatment modality for non-small-cell lung cancer (NSCLC), which accounts for approximately 85% of all lung cancer cases. Anti-PD-1/PD-L1 monoclonal antibodies have shown clinical efficacy by blocking the inhibitory interaction between PD-L1 on tumour cells and PD-1 on T cells, thereby restoring anti-tumour immune responses (Jeong et al., 2025). However, PD-L1 overexpression in NSCLC tumours represents one of the primary mechanisms by which cancer cells evade immune surveillance and suppress T cell-mediated cytotoxicity (Liu et al., 2025). Despite these advances, current antibody-based therapies face significant limitations including high production costs, immunogenicity in some patients, limited tissue penetration due to large molecular size (150–180 kDa), and variable patient response rates. These constraints have motivated the search for alternative therapeutic agents that can overcome these challenges while maintaining or improving efficacy (Amasawa et al., 2021).

Aptamers have emerged as promising alternatives to monoclonal antibodies for cancer immunotherapy. These short, single-stranded DNA or RNA oligonucleotides (typically 25–80 bases) can bind target molecules with high specificity and affinity through unique three-dimensional conformations. Through *in vitro* SELEX (Systematic Evolution of Ligands by Exponential Enrichment) processes, aptamers achieve binding capabilities comparable to those of antibodies, while offering several distinct advantages (Lee et al., 2023). Their smaller size (5–15 kDa) compared to antibodies (150–180 kDa) enables superior tissue and tumour penetration, particularly important for solid tumour like NSCLC. Aptamers demonstrate extended shelf-life stability under various environmental conditions, minimal batch-to-batch variation during synthesis, and extremely low immunogenicity. Additionally, they can be readily modified with chemical groups to enhance nuclease resistance, extend serum half-life, and enable targeted drug delivery, making them highly versatile for therapeutic applications.

From a therapeutic development perspective, aptamers offer significant practical advantages over antibodies. Aptamers are discovered through SELEX, an *in vitro* process requiring 2–8 weeks, whereas antibody development involves lengthier in vivo immunization protocols spanning several months to years (Lee et al., 2023). Aptamer production is highly scalable with minimal batch variation, ensuring consistent therapeutic performance and reducing manufacturing costs compared to monoclonal antibody production (Amasawa et al., 2021). While aptamers exhibit binding affinities in the nanomolar to picomolar range comparable to antibodies, they lack Fc-mediated effector functions inherent to monoclonal antibodies. However, unmodified aptamers are susceptible to nuclease degradation and have a limited *in vivo* half-life; nevertheless, chemical modifications, such as 2'-fluoropyrimidine incorporation, can effectively address these limitations and enhance stability.

Despite the promise of aptamer-based therapeutics, systematic design and *in vitro* validation of anti-PD-L1 aptamers for NSCLC treatment remains an active area of investigation. PD-L1 represents an attractive therapeutic target, as it is frequently overexpressed in NSCLC tumours, where it suppresses anti-tumour immunity by engaging with PD-1 on cytotoxic T cells, thereby facilitating immune evasion. Current monoclonal antibody-based PD-L1 blockade demonstrates clinical benefit in only a subset of patients, with acquired resistance mechanisms limiting therapeutic efficacy, highlighting the need for alternative therapeutic modalities. Computational approaches for aptamer design provide a rational and efficient strategy to identify high-affinity candidates before resource-intensive experimental validation, encompassing secondary structure prediction, tertiary structure optimization, molecular docking, and molecular dynamics simulation to assess binding stability and specificity. This study employed an integrated computational and experimental framework to design and validate a novel anti-PD-L1 aptamer (aptamer63) for NSCLC therapy. We performed *in silico* structure prediction and molecular dynamics simulation to design aptamer candidates targeting the PD-L1 binding interface, followed by comprehensive *in vitro* validation using NCI-H460 NSCLC cells. We systematically evaluated aptamer binding specificity, effects on cell proliferation and viability, induction of apoptosis, and capacity to enhance T cell-mediated cytotoxicity. This work establishes a rational computational-experimental design framework for developing aptamer-based immunotherapeutics targeting the PD-L1 checkpoint in NSCLC.

2. Methodology

2.1. Computational Design and Structural Characterisation of Anti-PD-L1 Aptamer

2.1.1. Target Protein Selection and Aptamer Design

The crystal structure of the PD-L1 protein was obtained from the Protein Data Bank (PDB ID: 6RPG) and processed for aptamer design using the EFBalite algorithm. The EFBalite program was utilised to

computationally generate candidate DNA aptamer sequences with predicted affinity for the PD-L1 binding interface.

2.1.2. Secondary Structure Prediction and Stability Analysis

Candidate aptamer sequences were analysed for secondary structure conformations using the MFold web server (http://www.mfold.org/mfold/applications/dna-folding-form.php) (Zuker, 2003). MFold predicts the thermodynamically favourable folding patterns of single-stranded nucleic acids by calculating minimum free energy states. Aptamer candidates demonstrating the most negative Gibbs free energy (ΔG) values were prioritised, as these values indicate greater conformational stability under physiological conditions.

2.1.3. Tertiary Structure Generation

The thermodynamically stable secondary structures were converted to RNA sequences and submitted to the 3dRNA v2.0 web server (http://biophy.hust.edu.cn/new/3dRNA/jobs/d86a0097-8232-4220-87a2-b89939cf1756) for three-dimensional architecture prediction (Zhang et al., 2020). The server generates multiple spatial conformations for each aptamer based on nucleotide arrangement templates. The model exhibiting the lowest structural score, indicative of optimal geometric quality, was selected for subsequent analysis. These RNA-based tertiary structures were then reconverted to DNA aptamer conformations using BIOVIA Discovery Studio Visualizer (Stasiewicz et al., 2019).

2.1.4. Molecular Docking Analysis

To evaluate binding modes and interaction strength between aptamer candidates and PD-L1, molecular docking simulations were conducted using HDOCK/ZDOCK servers (http://hdock.phys.hust.edu.cn/, https://zdock.umassmed.edu/) (Yan et al., 2017a). These platforms utilize rigid-body docking algorithms to predict the optimal configurations of aptamer-protein complexes. For each aptamer, the docking pose with the most favorable (most negative) binding score was selected, representing the configuration with the highest predicted binding affinity.

2.1.5. Binding Interaction Profiling

Detailed interaction mapping of the top-ranked aptamer-PD-L1 complexes was performed using the Protein-Ligand Interaction Profiler (PLIP) web server (https://plip-tool.biotec.tu-dresden.de/plip-web/plip/index) (Salentin et al., 2015). PLIP systematically identifies and classifies non-covalent binding interactions, including hydrogen bonding networks, hydrophobic contacts, electrostatic interactions (salt bridges), and aromatic π-stacking. This comprehensive binding profile provided insight into the molecular basis of aptamer specificity and affinity for PD-L1.

2.1.6. Molecular Dynamics Simulation

To evaluate the stability of the aptamer-PD-L1 complexes, molecular dynamics (MD) simulations were performed using Desmond (Schrödinger Release 2024). The top-ranked docking poses for aptamer63 and aptamer76 were prepared and solvated in a water box with appropriate counter ions. Production MD

simulations were conducted for 150 ns in the NVT ensemble at 300 K. Trajectory analysis was performed to calculate the root mean square deviation (RMSD) for assessing protein and aptamer stability. Protein-ligand interactions, including hydrogen bonds, hydrophobic contacts, ionic interactions, and water bridges, were monitored throughout the simulation. Interactions persisting for more than 30% of the simulation time were considered significant.

2.2. Validation of Aptamer63 Binding to NSCLC Cell Surface

To confirm the specific binding of aptamer63 to PD-L1 expressed on the surface of NSCLC cells, fluorescence microscopy analysis was performed using NCI-H460 cells. Briefly, 1×10^6 cells were seeded in 35 mm cell culture dishes and incubated overnight at 37°C with 5% CO_2 to allow for cell adherence. The cells were then treated with TAMRA (5-carboxytetramethylrhodamine)-labelled aptamer63 and incubated for 20 minutes. Following aptamer treatment, cells were stained with DAPI (4',6-diamidino-2-phenylindole) for 5 minutes in the dark for nuclear visualization. Fluorescence microscopy was performed to visualise the localisation of TAMRA-labelled aptamer63 on the cell surface and confirm binding specificity to NCI-H460 cells.

2.3 Cell Culture and Experimental Design

2.3.1 Cell Line and Culture Conditions

Human non-small cell lung cancer cell line NCI-H460 was obtained from the National Centre for Cell Science (NCCS), Pune, India. Cells were maintained in RPMI-1640 medium supplemented with 10% fetal bovine serum (FBS) and cultured at 37°C in a humidified incubator with 5% CO_2.

2.3.2 Experimental Group Assignments

To evaluate the therapeutic efficacy of aptamer63 in enhancing T cell-mediated cytotoxicity against NSCLC cells, six experimental groups were established. Group 1 served as the negative control and consisted of untreated NCI-H460 cells. Group 2 served as the positive control and comprised NCI-H460 cells co-cultured with activated T lymphocytes. Groups 3 through 6 consisted of NCI-H460 cells co-cultured with T lymphocytes in the presence of aptamer63 at concentrations of 50nM, 100nM, 150nM, and 200nM, respectively. This dose-response design enabled the systematic evaluation of aptamer63's concentration-dependent effect on T cell-mediated anti-tumour activity.

2.4 Assessment of T Cell-Mediated Cytotoxicity

2.4.1 Cell Proliferation Analysis by MTT Assay

To assess the effect of aptamer63 on NSCLC cell proliferation in the presence of activated T lymphocytes, the MTT (3-(4,5-dimethylthiazol-2-yl)-2,5-diphenyltetrazolium bromide) colorimetric assay was performed. NCI-H460 cells (5×10^3 cells/well) were seeded in 96-well plates and allowed to adhere for 24 hours. Cells were then treated with varying concentrations of aptamer63 (0, 50, 100, 150, and 200 nM) and incubated for 24 hours. Following aptamer treatment, activated T lymphocytes were added to

the wells and co-cultured for an additional 24 hours. The culture medium was then removed, and cells were washed with PBS. MTT solution (100 µL, 1 mg/mL) was added to each well, and plates were incubated in the dark for 4 hours at 37°C to allow formazan crystal formation. The MTT solution was subsequently removed, and the purple formazan crystals were dissolved in 100 µL dimethyl sulfoxide (DMSO). Absorbance was measured at 570 nm using a microplate reader, with cell proliferation expressed as a percentage relative to the untreated control.

2.4.2 Cell Viability Determination by Trypan Blue Exclusion Assay

Cell viability was assessed using the trypan blue dye exclusion method. NCI-H460 cells (5×10^3 cells/well) were seeded in 96-well plates and cultured for 24 hours. Cells were then treated with varying concentrations of aptamer63 and incubated for 24 hours, followed by the addition of T lymphocytes for an additional 24 hours. After the incubation period, cells were trypsinised and resuspended. An equal volume of cell suspension was mixed with 0.4% trypan blue dye. A 10 µL aliquot of the mixture was loaded into a Neubauer hemocytometer, and viable (unstained) and non-viable (blue-stained) cells were counted under a light microscope. Cell viability was calculated as the percentage of viable cells relative to the total number of cells.

2.4.3 Apoptosis Detection by Hoechst 33342/Propidium Iodide Dual Staining

To evaluate aptamer63-induced apoptosis in the presence of T lymphocytes, dual fluorescent staining with Hoechst 33342 and propidium iodide (PI) was performed. NCI-H460 cells (1×10^6 cells) were seeded in 35mm dishes and incubated overnight. Following treatment with varying concentrations of aptamer63 for 24 hours, activated T lymphocytes were added and co-cultured for an additional 24 hours. Cells were then stained with 500 µL of Hoechst 33342 (1 mg/mL) and incubated in the dark for 15 minutes to visualise nuclear morphology. Subsequently, 500 µL propidium iodide (1 mg/mL) was added and incubated for 15 minutes in the dark to identify necrotic cells with compromised membrane integrity (Cao et al., 2017; R & B, 2016). Apoptotic and necrotic cells were examined using fluorescence microscopy, with apoptotic cells characterised by condensed and fragmented nuclei.

2.4.4 Flow Cytometric Analysis of Cell Population

To quantify the effect of aptamer63 on total viable cell counts, flow cytometry analysis was performed. NCI-H460 cells (1×10^6 cells) were seeded in T-25 flasks (one flask per treatment group) and allowed to grow for 24 hours. Cells were treated with varying concentrations of aptamer63 for 24 hours, followed by the addition of activated T lymphocytes and overnight incubation. The cells were then washed twice with 1× PBS, trypsinized, and resuspended. Propidium iodide (10 µL, 1 mg/mL) was added to each sample and incubated in the dark to stain non-viable cells. Cell populations were analyzed using flow cytometry, and the percentage of viable cells (PI-negative) was quantified.

3. Results and Discussion

3.1. Computational Design and Structural Characterisation of Anti-PD-L1 Aptamer

3.1.1. Target Protein Selection and Aptamer Design

Following the computational design protocol, multiple anti-PD-L1 aptamer candidates were generated using the EFBalite algorithm against the PD-L1 protein (PDB ID: 6RPG). Based on predicted binding affinity and structural features, two aptamer sequences, designated as aptamer63 and aptamer76, were selected for comprehensive structural and functional characterisation.

3.1.2. Secondary Structure Prediction and Stability Analysis

Secondary structure prediction using the MFold web server revealed distinct folding patterns for both aptamers, as shown in Figures 1 (a) and (b). Aptamer63 exhibited a Gibbs free energy (ΔG) of -3.66 kcal/mol, while aptamer76 displayed a ΔG of -3.06 kcal/mol. The more negative ΔG value of aptamer63 indicates greater thermodynamic stability, suggesting a more favourable secondary structure conformation under physiological conditions.

3.1.3. Tertiary Structure Generation

The predicted secondary structures of both aptamers were subsequently converted to RNA sequences and submitted to the 3dRNA v2.0 web server for three-dimensional structure prediction. For each aptamer, the server generated five distinct tertiary structure models with varying structural scores. The models with the lowest scores were selected for aptamer63 (score: 25.7888) and aptamer76 (score: 26.1852), as illustrated in Figure 1 (c) and (d). Lower structural scores indicate superior geometric quality and conformational stability. Following tertiary structure prediction, the RNA-based models were reconverted to DNA conformations using BIOVIA Discovery Studio Visualizer for subsequent docking analysis.

3.1.4. Molecular Docking Analysis

The optimised tertiary structures of aptamer63 and aptamer76 were subjected to molecular docking analysis using HDOCK and ZDOCK web servers to predict their binding modes with the PD-L1 protein. For each aptamer, multiple docking poses were generated, and the conformation with the most favourable (most negative) docking score was selected for further analysis. Docking scores represent the predicted change in binding free energy upon complex formation between the aptamer (ligand) and PD-L1 protein (target). More negative scores indicate stronger predicted binding affinity and greater thermodynamic stability of the aptamer-protein complex, whereas less negative or positive scores suggest weak or negligible binding interactions. Thus, selection of the minimum docking score ensures identification of the most stable and energetically favorable binding configuration.

Detailed characterisation of molecular interactions at the binding interface was performed using the Protein-Ligand Interaction Profiler (PLIP) web server. The analysis revealed multiple types of non-covalent interactions stabilising the aptamer-PD-L1 complexes, as summarised in Table 1. Both aptamers exhibited a predominance of hydrogen bonding interactions with PD-L1 residues. Notably, aptamer63 formed 14 hydrogen bonds via HDOCK and 7 via ZDOCK, while aptamer76 formed 13 and 15 hydrogen bonds, respectively. Hydrogen bonding is a crucial determinant of ligand-binding specificity and affinity, significantly contributing to the structural complementarity and stability of the aptamer-protein interface. Additionally, hydrophobic contacts, salt bridges, and π-stacking interactions were observed, further enhancing the binding stability. Aptamer63 demonstrated a higher total number of interactions (22 via HDOCK) compared to aptamer76 (20 via HDOCK), suggesting superior binding affinity and selectivity for PD-L1.

Table 1. Interaction profile of aptamer-PD-L1 complexes from molecular docking analysis. Summary of non-covalent interactions identified between anti-PD-L1 aptamers (aptamer63 and aptamer76) and PD-L1 protein using PLIP analysis. Interactions include hydrogen bonds, hydrophobic contacts, salt bridges, and π-stacking. Aptamer63 exhibits a higher total number of interactions via HDOCK (22) compared to aptamer76 (20), suggesting stronger predicted binding affinity.

Name	Docking	Hydrogen bond	Hydrophobic bond	Salt bridges	π-Stacking	Total number of interactions
Aptamer63	HDOCK	14	4	3	1	22
	ZDOCK	7	4	-	-	11
Aptamer76	HDOCK	13	3	3	1	20
	ZDOCK	15	2	-	-	17

3.1.5 Molecular Dynamics Simulation

To validate the stability and binding characteristics of the aptamer-PD-L1 complexes under physiological conditions, 150 ns molecular dynamics simulations were conducted for both aptamer63 and aptamer76.

RMSD Analysis of Structural Stability

Root mean square deviation (RMSD) analysis revealed that both the PD-L1 protein and aptamer63 maintained stable conformations throughout the simulation. As shown in Figure 2, the protein backbone RMSD fluctuated between 1-3 Å, which is within the acceptable range for small globular proteins and indicates structural equilibration. The aptamer63 RMSD remained stable relative to the protein binding pocket, with fluctuations that did not significantly exceed the protein RMSD. This indicates that aptamer63 retained its binding position without diffusing away from the initial docking site, confirming the stability of the aptamer-protein complex.

Protein-Ligand Interaction Analysis

Detailed interaction profiling throughout the MD trajectory identified key residues responsible for aptamer63 binding stability (Figure 3). Interactions persisting for more than 30% of the simulation duration were considered significant contributors to binding affinity. The analysis revealed four major types of stabilizing interactions: hydrogen bonds, hydrophobic contacts, ionic interactions, and water-mediated bridges. Aptamer63 exhibited sustained hydrogen bonding and hydrophobic interactions with PD-L1 residues, contributing to enhanced binding stability compared to aptamer76. Hydrophobic interactions between aptamer nucleotides and the hydrophobic amino acids of PD-L1 further stabilised the protein-ligand interface.

Comparative Analysis and Aptamer Selection

Table 2 presents a comprehensive comparison of interaction profiles for aptamer63 and aptamer76 before and after MD simulation. Post-simulation analysis demonstrated that aptamer63 maintained a higher total number of interactions with PD-L1 across both chains (A and B) compared to aptamer76. Specifically, aptamer63 showed increased nucleotide-residue interactions (50 interactions in chain B), higher hydrogen bond counts (12 H-bonds in chain B), and more favourable hydrophobicity scores (-0.75 for chain B). The LigPlot analysis in Figure 4 further confirmed that aptamer63 forms stable hydrogen bonds with Pro133 and Glu60 via guanine residues at positions 8 and 18, while engaging in hydrophobic bonding with Asp61, Tyr134, and Ala132 through thymine residues at positions 9, 10, 19, and 20.

Table 2. Comparative interaction analysis before and after MD simulation. Summary of protein-ligand interactions for aptamer63 and aptamer76 before (docking) and after (150 ns MD simulation) with PD-L1 protein chains A and B. Parameters include nucleotide-residue interactions, hydrogen bonds, van der Waals contacts, hydrophobicity scores, and secondary structure composition. Aptamer63 exhibits superior interaction profiles post-simulation, supporting its selection for experimental validation.

Name	Simulation	Pro. Chain ID	Nuc-Res Interactions	Weak Nuc-Res Interaction	Total interactions	Total H-bond	Total vdW	Hydrophobicity Score	Secondary Structure Composition
Aptamer63	Before	A	8	0	8	2	32	0.36	irregular
		B	42	3	45	10	114	-0.166	helix/strand
	After	A	34	1	35	11	77	-1.246	irregular
		B	50	2	52	12	87	-0.75	strand
Aptamer76	Before	A	8	0	8	2	31	0.36	irregular
		B	43	3	46	10	113	-0.125	helix/strand
	After	A	33	1	34	6	67	-0.081	helix/strand
		B	35	5	40	14	84	0.39	helix/strand

3.2 Aptamer63 Specifically Binds to PD-L1 on NCI-H460 Cell Surface

To experimentally validate the predicted binding affinity of aptamer63 for PD-L1, fluorescence microscopy was performed using TAMRA-labelled aptamer63 on NCI-H460 NSCLC cells. As shown in Figure 5(a), red fluorescence signal from TAMRA-labelled aptamer63 was clearly detected on the cell surface, indicating successful aptamer binding. Figure 5(b) shows DAPI-stained cell nuclei (blue fluorescence), confirming cell integrity and providing nuclear localisation. The merged image in Figure 5(c) demonstrates the spatial relationship between nuclear staining and cell surface-bound aptamer, with red fluorescence localised at the cell periphery surrounding the blue-stained nuclei. This pattern confirms that aptamer63 specifically binds to PD-L1 expressed on the NCI-H460 cell surface rather than non-specifically internalising or binding to intracellular components. The absence of red fluorescence in the nuclear region and its concentration at the cell membrane validate the membrane-localised binding of aptamer63 to PD-L1, consistent with the known cell surface expression of PD-L1 on NSCLC cells.

3.3 Aptamer63 Enhances T Cell-Mediated Inhibition of NSCLC Cell Proliferation

To evaluate the functional impact of aptamer63 on T cell-mediated anti-tumour activity, cell proliferation was assessed using the MTT assay, which measures metabolic activity as an indicator of viable cell

number. As shown in Figure 5(d), untreated NCI-H460 cells exhibited baseline proliferation levels (100%). Treatment with activated T lymphocytes alone resulted in a modest reduction in cell proliferation to approximately 80% ($p < 0.05$), indicating some degree of T cell-mediated cytotoxicity against NSCLC cells.

Importantly, co-treatment with aptamer63 significantly enhanced the anti-proliferative effects of T lymphocytes in a concentration-dependent manner. At 50nM aptamer63 concentration, cell proliferation decreased to approximately 70% ($p < 0.05$), demonstrating a statistically significant enhancement compared to untreated controls. The most pronounced inhibition of cell proliferation was observed at 100 nM aptamer63, where proliferation was reduced to approximately 68% ($p < 0.05$). Higher concentrations of aptamer63 (150nM and 200nM) maintained similar levels of proliferation inhibition (~75-80%), though these did not achieve statistical significance relative to controls.

These findings demonstrate that aptamer63 potentiates T cell-mediated cytotoxicity against NCI-H460 cells, with optimal efficacy observed at 100nM concentration. By blocking PD-L1 on the tumour cell surface, aptamer63 appears to relieve immunosuppressive signalling, thereby enhancing T lymphocyte effector function and tumour cell killing. The statistically significant reduction in cell proliferation ($p < 0.05$) at lower aptamer concentrations provides quantitative evidence that aptamer63 can restore T cell cytotoxic activity that would otherwise be suppressed by PD-L1/PD-1 interactions.

3.4 Aptamer63 Significantly Reduces Cell Viability in T Cell Co-Culture

Cell viability was directly assessed using the trypan blue exclusion assay, which distinguishes viable cells (with intact membrane integrity) from non-viable cells (with compromised membranes). Trypan blue dye selectively penetrates cells with damaged membranes, allowing for direct enumeration of live versus dead cells. Following the same treatment regimen as the MTT assay, NCI-H460 cells were stained with trypan blue and counted using a Neubauer hemocytometer. Viable cells appeared transparent, while dead cells exhibited blue colouration due to dye uptake.

As shown in Figure 6, untreated NCI-H460 cells maintained approximately 92% viability. Treatment with activated T lymphocytes alone significantly reduced viability to approximately 65% ($*p < 0.01$), demonstrating baseline T cell-mediated cytotoxicity. Co-treatment with 50 nM aptamer63 showed similar viability (~62%, $*p < 0.01$) to that of T lymphocytes alone, suggesting minimal enhancement at this lower concentration. However, at 100 nM aptamer63, cell viability was dramatically reduced to approximately 20% ($***p < 0.0001$), representing a greater than 3-fold enhancement of T cell cytotoxicity compared to T lymphocytes alone. At 150 nM, viability increased to ~62% ($*p < 0.01$), while at 200 nM, viability was reduced to approximately 30%$*p < 0.0001$).

The exceptionally low p-values ($p < 0.0001$) for 100nM and 200nM concentrations demonstrate highly significant and reproducible effects. The dramatic reduction in viable cell counts, particularly at 100nM, confirms that aptamer63 potently enhances T lymphocyte-mediated killing of NCI-H460 cells. These findings provide direct quantitative evidence that aptamer63-mediated PD-L1 blockade restores T cell

cytotoxic function, resulting in substantial tumour cell death. The 100nM concentration was found to be the optimal dose, resulting in the maximal enhancement of T cell-mediated cytotoxicity.

3.5 Aptamer63 Induces Apoptosis and Necrosis in T Cell-Treated NSCLC Cells

To visualise and characterise the mode of cell death induced by aptamer63-enhanced T cell therapy, Hoechst 33342/propidium iodide (PI) dual fluorescence staining was performed. Hoechst 33342 is a cell-permeable nuclear dye that stains all cell nuclei blue, allowing differentiation between viable cells (diffuse, uniform nuclear staining) and apoptotic cells (condensed, fragmented, or brightly fluorescent nuclei). Propidium iodide is membrane-impermeant and selectively stains cells with compromised membrane integrity, specifically necrotic and late-stage apoptotic cells, producing red fluorescence.

As shown in Figure 7, untreated control cells displayed predominantly diffuse blue nuclear staining with minimal red PI fluorescence, indicating healthy, viable cells with intact nuclear morphology and membrane integrity. T lymphocyte treatment alone induced modest increases in both apoptotic nuclear morphology (condensed bright blue nuclei) and necrotic cell death (red PI-positive cells).

Co-treatment with aptamer63 markedly enhanced both apoptotic and necrotic cell death in a concentration-dependent manner. At 50nM aptamer63, a noticeable increase in condensed, fragmented nuclei (apoptosis) and PI-positive cells (necrosis) was observed compared to T lymphocytes alone. The 100nM concentration produced the most dramatic effect, displaying extensive bright blue condensed nuclei characteristic of widespread apoptosis, along with the highest intensity of red PI fluorescence, indicating substantial necrotic cell death. The merged images at 100 nM showed pronounced purple/pink colouration, reflecting co-localisation of nuclear condensation and membrane permeabilisation. At 150nM and 200nM concentrations, increased cell death was also evident, though the visual intensity appeared somewhat reduced compared to the 100nM treatment.

These microscopic observations confirm that aptamer63 enhances T cell-mediated tumour cell killing through induction of both apoptotic and necrotic pathways. The 100 nM concentration consistently demonstrated maximal cytotoxic efficacy, corroborating the quantitative findings from MTT and trypan blue assays. The presence of both apoptotic (condensed nuclei) and necrotic (PI-positive) cells suggests that aptamer63-mediated PD-L1 blockade enables T lymphocytes to induce multiple cell death pathways, resulting in comprehensive elimination of tumour cells.

3.6 Flow Cytometry Confirms Maximum T Cell Cytotoxicity at 100nM Aptamer63

To quantitatively assess the viable cell population following treatment, flow cytometry analysis was performed using forward scatter (FSC) and side scatter (SSC) parameters, which provide information on cell size and internal complexity, respectively. Viable cells with intact morphology were identified and gated in region R1 on FSC-SSC dot plots (Figure 8(a)), while cell debris, dead cells, and cellular fragments appeared outside this gated region due to their altered size and granularity characteristics.

Figure 8(a) demonstrates representative dot plots for each treatment group. The untreated control and T lymphocyte-treated samples showed relatively dense populations within the R1 gate, indicating high proportions of viable cells. In contrast, samples co-treated with aptamer63 and T lymphocytes exhibited noticeably reduced cell populations within the R1 gate, with increased scatter events outside the gated region, indicative of enhanced cell death and debris formation.

Quantitative analysis of the gated cell populations is presented in Figure 8(b). Untreated control cells showed approximately 100% gating within R1, representing the baseline viable cell population. T lymphocyte treatment alone reduced the gated population to approximately 86%, consistent with modest baseline T cell cytotoxicity. Co-treatment with aptamer63 produced significant, concentration-dependent reductions in viable cell counts. At 50 nM aptamer63, the gated population decreased to approximately 66%. The most pronounced effect was observed at 100 nM, where only 63% of cells fell within the viable cell gate, representing a reduction of approximately 27% compared to T lymphocytes alone (***$p < 0.0001$). At 150 nM and 200 nM concentrations, gated populations were approximately 65% and 68%, respectively, indicating slightly reduced efficacy compared to the 100 nM dose.

The highly significant p-value (***$p < 0.0001$) for aptamer63 treatments confirms that the observed reductions in viable cell populations are statistically robust and reproducible. The 100 nM concentration consistently demonstrated the lowest percentage of viable cells (63%), corroborating findings from MTT, trypan blue, and Hoechst/PI assays. Collectively, these flow cytometry data provide quantitative validation that aptamer63 at 100 nM optimally enhances T cell-mediated elimination of NCI-H460 cells, establishing this concentration as the most effective dose for PD-L1 blockade-enhanced immunotherapy.

4. Conclusion

The study combined computational design and experimental validation to develop aptamer63, a novel DNA aptamer targeting PD-L1 for enhanced immunotherapy in non-small cell lung cancer (NSCLC). Through systematic *in silico* screening, we identified aptamer63 as having superior structural stability (ΔG = -3.66 kcal/mol) and optimal binding affinity to PD-L1 compared to other candidates. Molecular docking studies revealed that aptamer63 forms 22 distinct interactions with PD-L1, including hydrogen bonds, hydrophobic contacts, salt bridges, and π-stacking interactions, primarily involving key residues Pro133, Glu60, Asp61, Tyr134, and Ala132. Molecular dynamics simulation over 150 ns confirmed the stability of the aptamer63-PD-L1 complex under physiological conditions, with RMSD values remaining within acceptable ranges (1–3 Å), validating the predicted binding mode.

In vitro validation using NCI-H460 NSCLC cells demonstrated that aptamer63 specifically binds to the cell surface PD-L1, as confirmed by fluorescence microscopy. Functional assays across multiple platforms—MTT, trypan blue exclusion, Hoechst/PI dual staining, and flow cytometry—consistently identified 100 nM as the optimal aptamer63 concentration for enhancing T cell-mediated cytotoxicity. At this concentration, aptamer63 reduced cell viability to approximately 20% (trypan blue assay) and

decreased the viable gated cell population to 63% (flow cytometry), representing significant improvements over T lymphocyte treatment alone (***$p < 0.0001$). Importantly, aptamer63 induced both apoptotic and necrotic cell death pathways, indicating comprehensive tumour cell elimination through multiple mechanisms.

Our findings thus established aptamer63 as a promising candidate for PD-L1-targeted immunotherapy in NSCLC. The integration of computational prediction with rigorous *in vitro* validation provides a robust framework for aptamer development, positioning aptamer63 for advancement to preclinical *in vivo* studies.

KTR conceptualised the study and provided the initial outline of the manuscript. PKM conducted data collection, performed experimental work in collaboration with YS, and prepared the primary manuscript draft. YS contributed to image generation and data analysis. KTR carried out the final review, editing, and evaluation of the manuscript. All authors contributed to the interpretation of results, reviewed the manuscript critically for important intellectual content, and approved the final version for submission.

Declarations

Funding: This research received no specific grant from public, commercial, or not-for-profit funding agencies.

Conflict of interests: The authors report no conflict of interest.

Ethical approval: This article does not contain any studies with human participants or animals performed by the authors.

Funding:

This research received no specific grant from public, commercial, or not-for-profit funding agencies.

Author Contribution

KTR conceptualised the study and provided the initial outline of the manuscript. PKM conducted data collection, performed experimental work in collaboration with YS, and prepared the primary manuscript draft. YS contributed to image generation and data analysis. KTR carried out the final review, editing, and evaluation of the manuscript. All authors contributed to the interpretation of results, reviewed the manuscript critically for important intellectual content, and approved the final version for submission.

References

1. Ai, X., Jia, B., He, Z., Zhang, J., Zhuo, M., Zhao, J., Wang, Z., Zhang, J., Fan, Z., Zhang, X., Li, C., Jin, F., Li, Z., Ma, X., Tang, H., Yan, X., Li, W., Xiong, Y., Yin, H., … Lu, S. (2024). Noninvasive early identification of durable clinical benefit from immune checkpoint inhibition: a prospective multicenter study (NCT04566432). *Signal Transduction and Targeted Therapy 2024 9:1*, *9*(1), 350-. https://doi.org/10.1038/s41392-024-02060-3
2. Amasawa, E., Kuroda, H., Okamura, K., Badr, S., & Sugiyama, H. (2021). Cost–Benefit Analysis of Monoclonal Antibody Cultivation Scenarios in Terms of Life Cycle Environmental Impact and Operating Cost. *ACS Sustainable Chemistry & Engineering*, *9*(42), 14012–14021. https://doi.org/10.1021/ACSSUSCHEMENG.1C01435
3. *Global cancer burden growing, amidst mounting need for services*. Retrieved November 25, 2025, from https://www.who.int/news/item/01-02-2024-global-cancer-burden-growing--amidst-mounting-need-for-services
4. Jeong, H., Koh, J., Kim, S., Yim, J., Song, S. G., Kim, H., Li, Y., Lee, S. H., Chung, Y. K., Kim, H., Lee, C. H., Kim, H. Y., Keam, B., Lee, S. H., Chung, D. H., & Jeon, Y. K. (2025). Cell-intrinsic PD-L1 signaling drives immunosuppression by myeloid-derived suppressor cells through IL-6/Jak/Stat3 in PD-L1-high lung cancer. *Journal for ImmunoTherapy of Cancer*, *13*(3). https://doi.org/10.1136/JITC-2024-010612
5. Lee, S. J., Cho, J., Lee, B. H., Hwang, D., & Park, J. W. (2023). Design and Prediction of Aptamers Assisted by In Silico Methods. *Biomedicines*, *11*(2), 356. https://doi.org/10.3390/BIOMEDICINES11020356
6. Lim, S. M., Hong, M. H., & Kim, H. R. (2020). Immunotherapy for Non-small Cell Lung Cancer: Current Landscape and Future Perspectives. *Immune Network*, *20*(1), e10. https://doi.org/10.4110/IN.2020.20.E10
7. Liu, J., Cai, Y., Liu, J., Chen, D., & Wu, X. (2025). Immunotherapy Resistance and Therapeutic Strategies in PD-L1 High Expression Non-Small Cell Lung Cancer. *OncoTargets and Therapy*, *18*, 953. https://doi.org/10.2147/OTT.S539978
8. Salentin, S., Schreiber, S., Haupt, V. J., Adasme, M. F., & Schroeder, M. (2015). PLIP: fully automated protein-ligand interaction profiler. *Nucleic Acids Research*, *43*(W1), W443–W447. https://doi.org/10.1093/NAR/GKV315
9. Stasiewicz, J., Mukherjee, S., Nithin, C., & Bujnicki, J. M. (2019). QRNAS: software tool for refinement of nucleic acid structures. *BMC Structural Biology*, *19*(1). https://doi.org/10.1186/S12900-019-0103-1
10. Yan, Y., Zhang, D., Zhou, P., Li, B., & Huang, S. Y. (2017). HDOCK: a web server for protein-protein and protein-DNA/RNA docking based on a hybrid strategy. *Nucleic Acids Research*, *45*(W1), W365–W373. https://doi.org/10.1093/NAR/GKX407
11. Zhang, Y., Wang, J., & Xiao, Y. (2020). 3dRNA: Building RNA 3D structure with improved template library. *Computational and Structural Biotechnology Journal*, *18*, 2416. https://doi.org/10.1016/J.CSBJ.2020.08.017

12. Zuker, M. (2003). Mfold web server for nucleic acid folding and hybridization prediction. *Nucleic Acids Research*, *31*(13), 3406–3415. https://doi.org/10.1093/NAR/GKG595

Figures

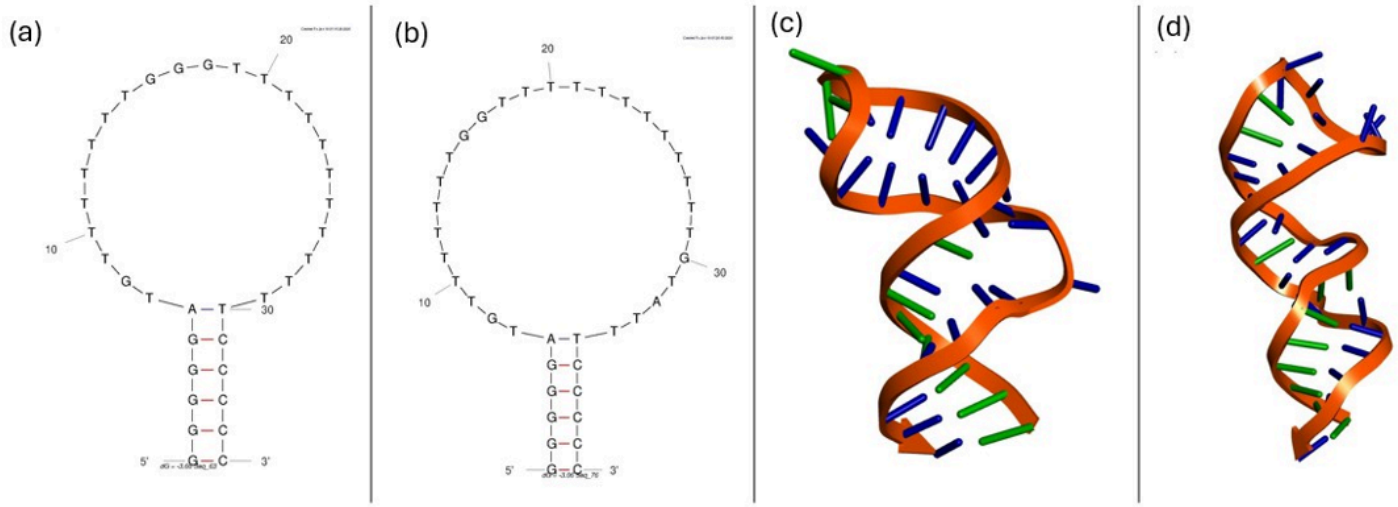

Figure 1

Secondary and tertiary structure prediction of anti-PD-L1 aptamers. MFold-predicted secondary structures and 3dRNA v2.0-generated tertiary models for (a, c) aptamer63 and (b, d) aptamer76. Aptamer63 shows superior thermodynamic stability (ΔG = -3.66 kcal/mol, structural score = 25.7888) compared to aptamer76 (ΔG = -3.06 kcal/mol, score = 26.1852). In 3D models, the sugar-phosphate backbone is shown in orange, pyrimidines in blue, and purines in green.

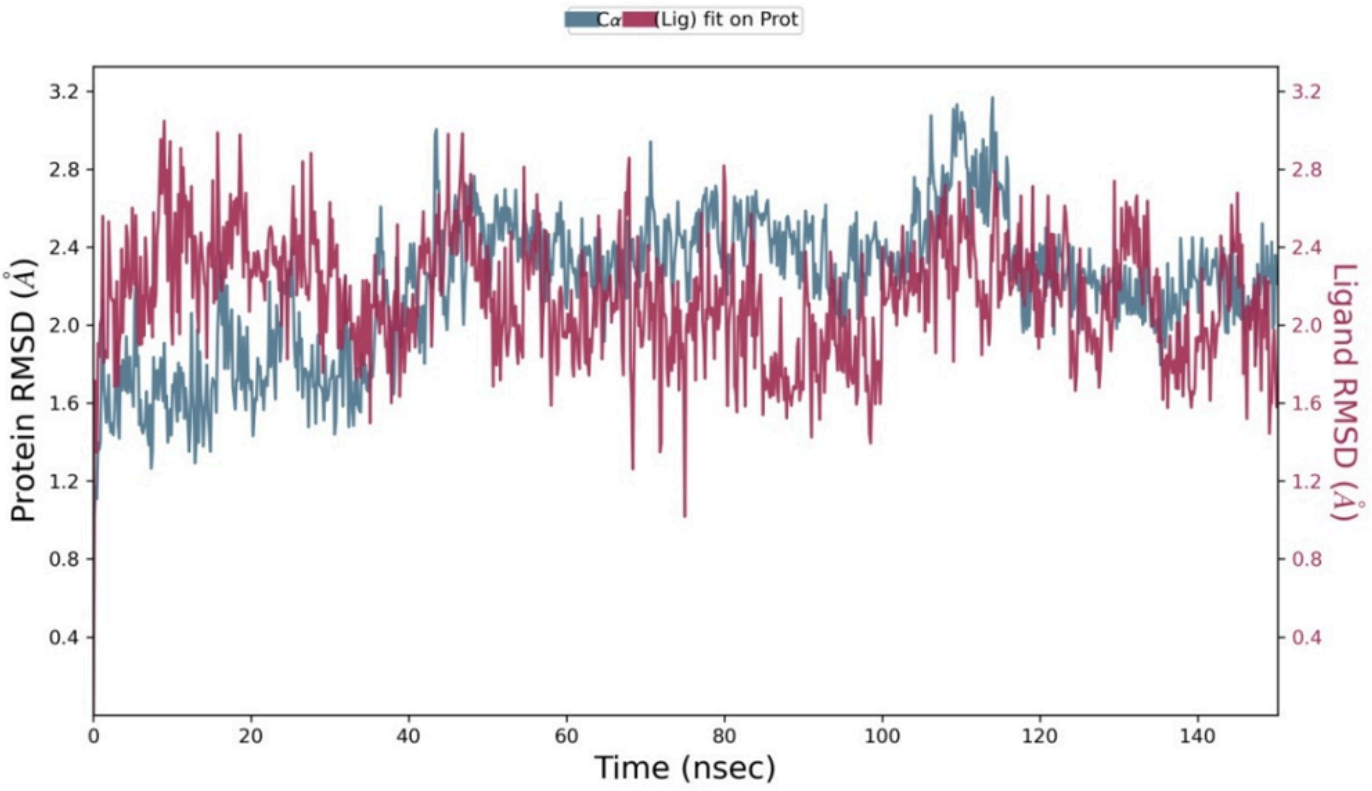

Figure 2

RMSD analysis of protein-ligand complex stability during MD simulation. RMSD plot showing the structural stability of PD-L1 protein (left Y-axis) and aptamer63 (right Y-axis) over the 150 ns simulation trajectory. Protein backbone RMSD values range from 1-3 Å, indicating acceptable structural fluctuations. Aptamer RMSD remains stable relative to the binding pocket, confirming that the ligand maintains its binding position throughout the simulation.

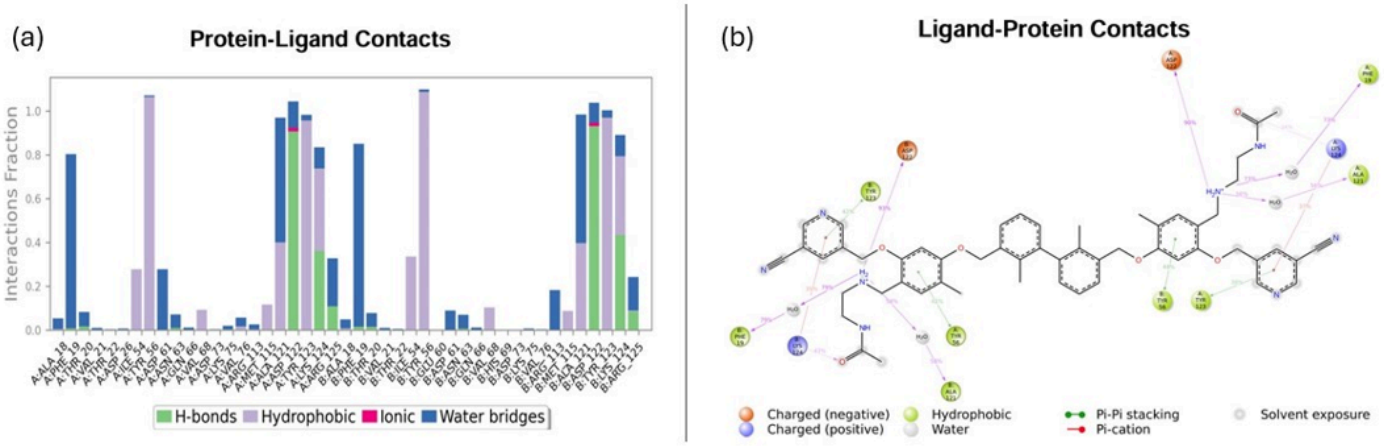

Figure 3

Aptamer63-PD-L1 interaction analysis from MD simulation. Interaction profile showing (a) histogram of contact frequencies for hydrogen bonds, hydrophobic contacts, ionic interactions, and water bridges with individual PD-L1 residues over 150 ns simulation, and (b) 2D contact map highlighting key stabilizing interactions (charged, hydrophobic, water-mediated, pi-pi stacking, and pi-cation) between aptamer63 and PD-L1 residues.

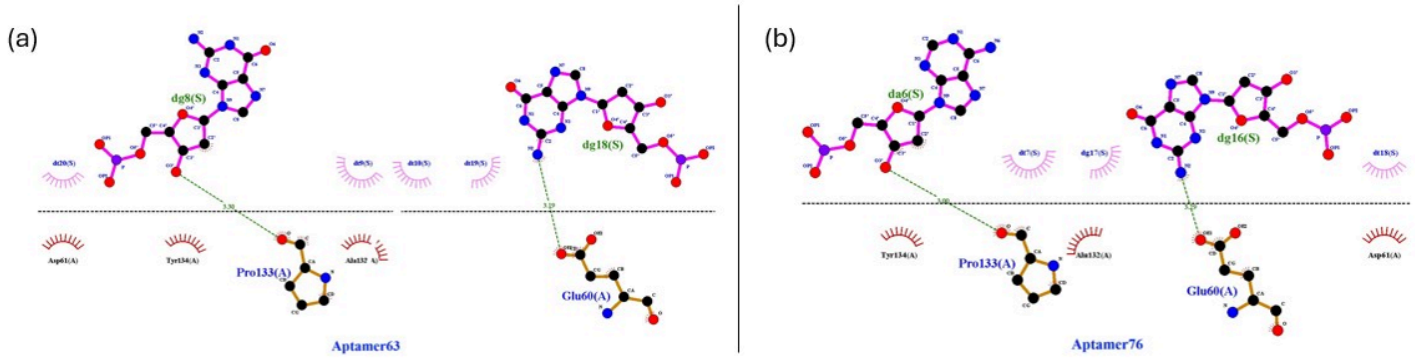

Figure 4

LigPlot analysis of aptamer-PD-L1 binding interactions. Two-dimensional interaction diagrams showing hydrogen bonding (dashed lines) and hydrophobic contacts (arc patterns) between (a) aptamer63 and (b) aptamer76 with PD-L1 residues. Aptamer63 demonstrates more extensive and stable interactions, particularly with Pro133, Glu60, Asp61, Tyr134, and Ala132, indicating stronger predicted binding affinity.

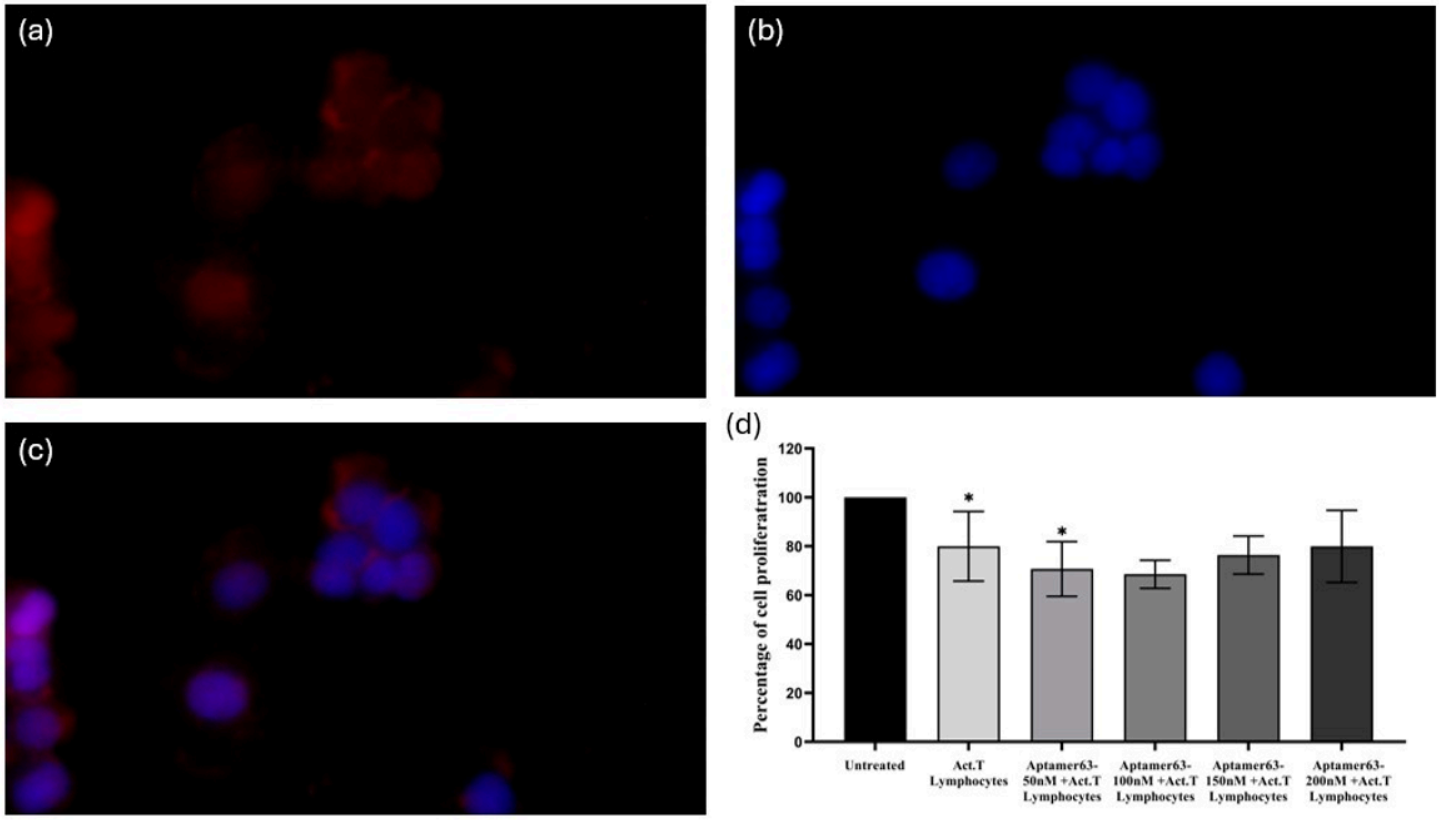

Figure 5

Aptamer63 binding validation and functional efficacy in NSCLC cells. (a-c) Fluorescence microscopy validation of aptamer63 binding to NCI-H460 cells:(a) TAMRA-labelled aptamer63 showing red fluorescence at the cell surface (excitation: 552 nm), (b) DAPI-stained nuclei showing blue fluorescence (excitation: 358 nm), and (c) merged image demonstrating aptamer63 localisation at the cell periphery, confirming specific PD-L1 surface binding. Scale bar: 10μm; magnification: 40×. **(d) T cell-mediated cytotoxicity enhancement:** MTT assay showing cell proliferation (%) after 24-hour treatment with aptamer63 (50, 100, 150, 200nM) plus activated T lymphocytes. Aptamer63 at 50-100nM significantly enhanced T cell-mediated growth inhibition compared to T lymphocytes alone. Data represent mean ± SD. *p < 0.05 compared to untreated control.

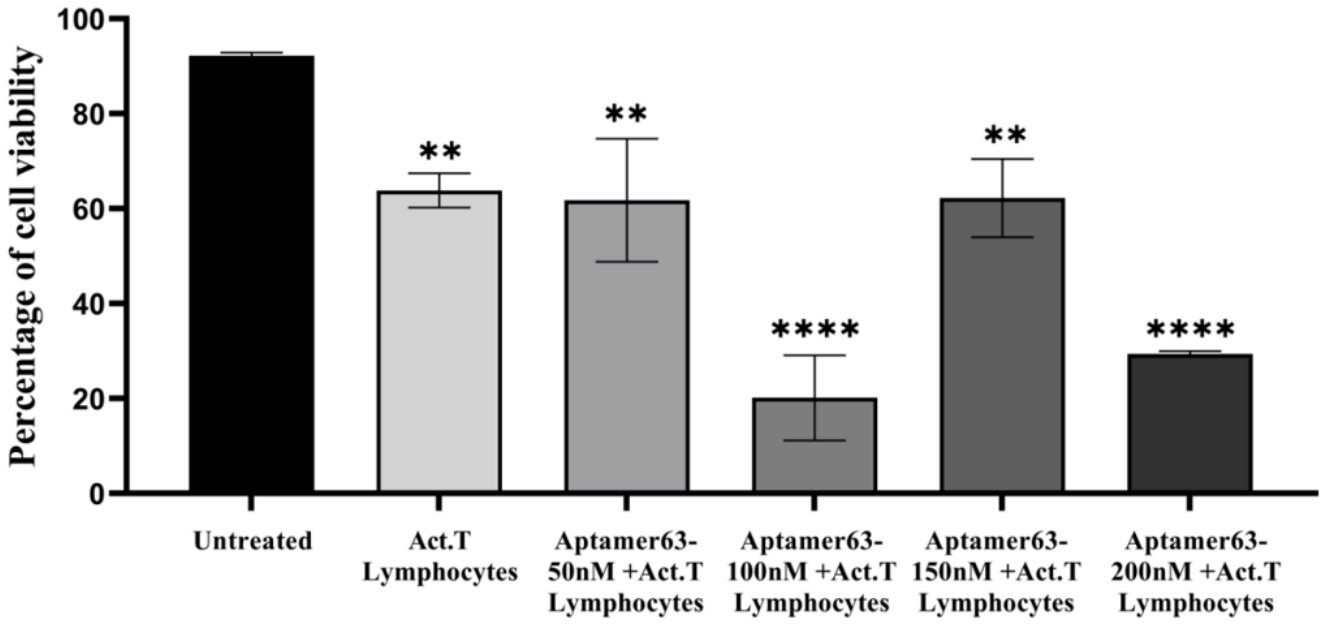

Figure 6

Aptamer63 dramatically enhances T cell-mediated cytotoxicity against NCI-H460 cells. Trypan blue exclusion assay results showing percentage of viable cells after treatment with varying concentrations of aptamer63 (50, 100, 150, and 200 nM) in combination with activated T lymphocytes. Live cells with intact membranes exclude trypan blue and remain transparent, while dead cells with compromised membranes take up the dye and appear blue. Aptamer63 at 100nM concentration achieved the most dramatic reduction in viability (~20%), representing optimal enhancement of T cell cytotoxicity. Data represent mean ± SD. *p < 0.01, ***p < 0.0001 compared to untreated control.

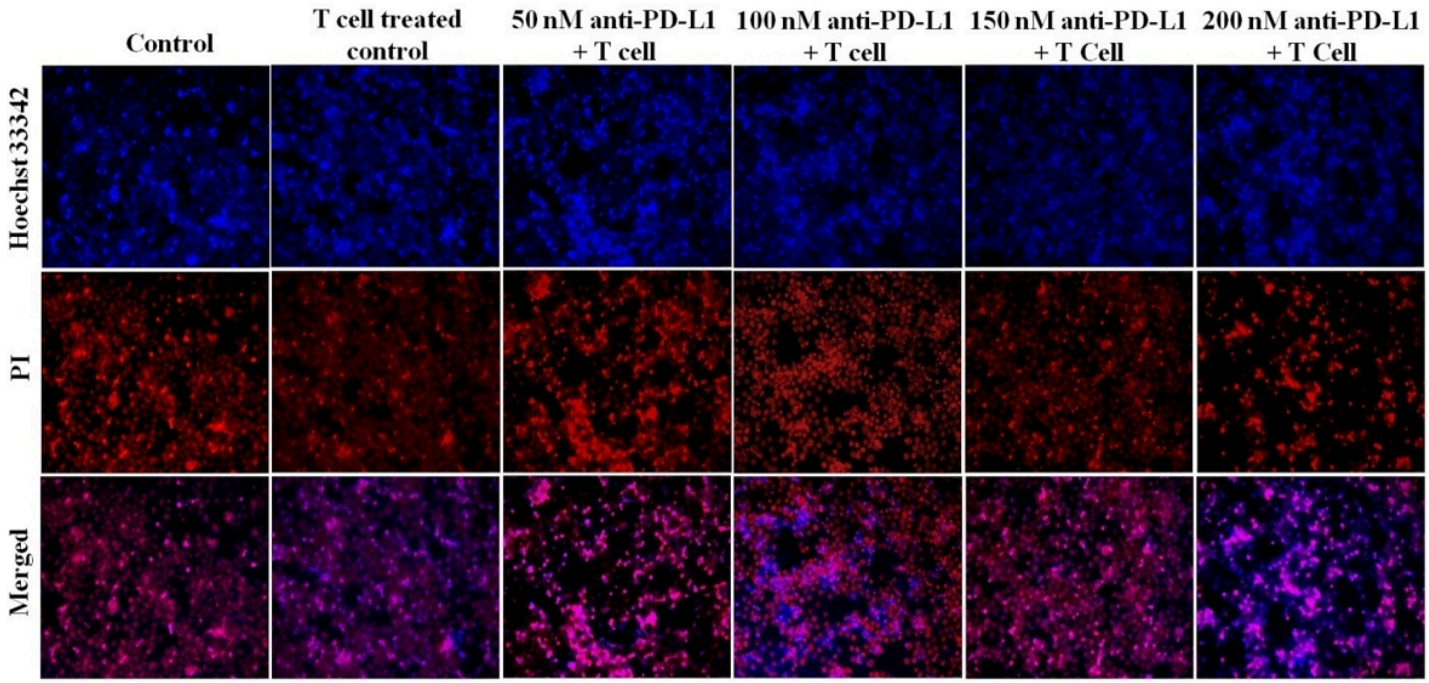

Figure 7

Aptamer63 induces apoptosis and necrosis in NCI-H460 cells during T cell co-culture. Representative fluorescence microscopy images of NCI-H460 cells after 24-hour treatment with varying concentrations of aptamer63 (50, 100, 150, and 200 nM) in combination with activated T lymphocytes. Top row: Hoechst 33342 staining (blue) shows nuclear morphology; condensed, fragmented, or brightly stained nuclei indicate apoptosis. Middle row: Propidium iodide (PI) staining (red) identifies necrotic cells with compromised membrane integrity. Bottom row: Merged images showing co-localization of apoptotic and necrotic markers. The 100 nM aptamer63 concentration demonstrates the most extensive cell death, characterised by widespread nuclear condensation and high PI uptake, validating this concentration as optimal for enhancing T cell-mediated cytotoxicity.

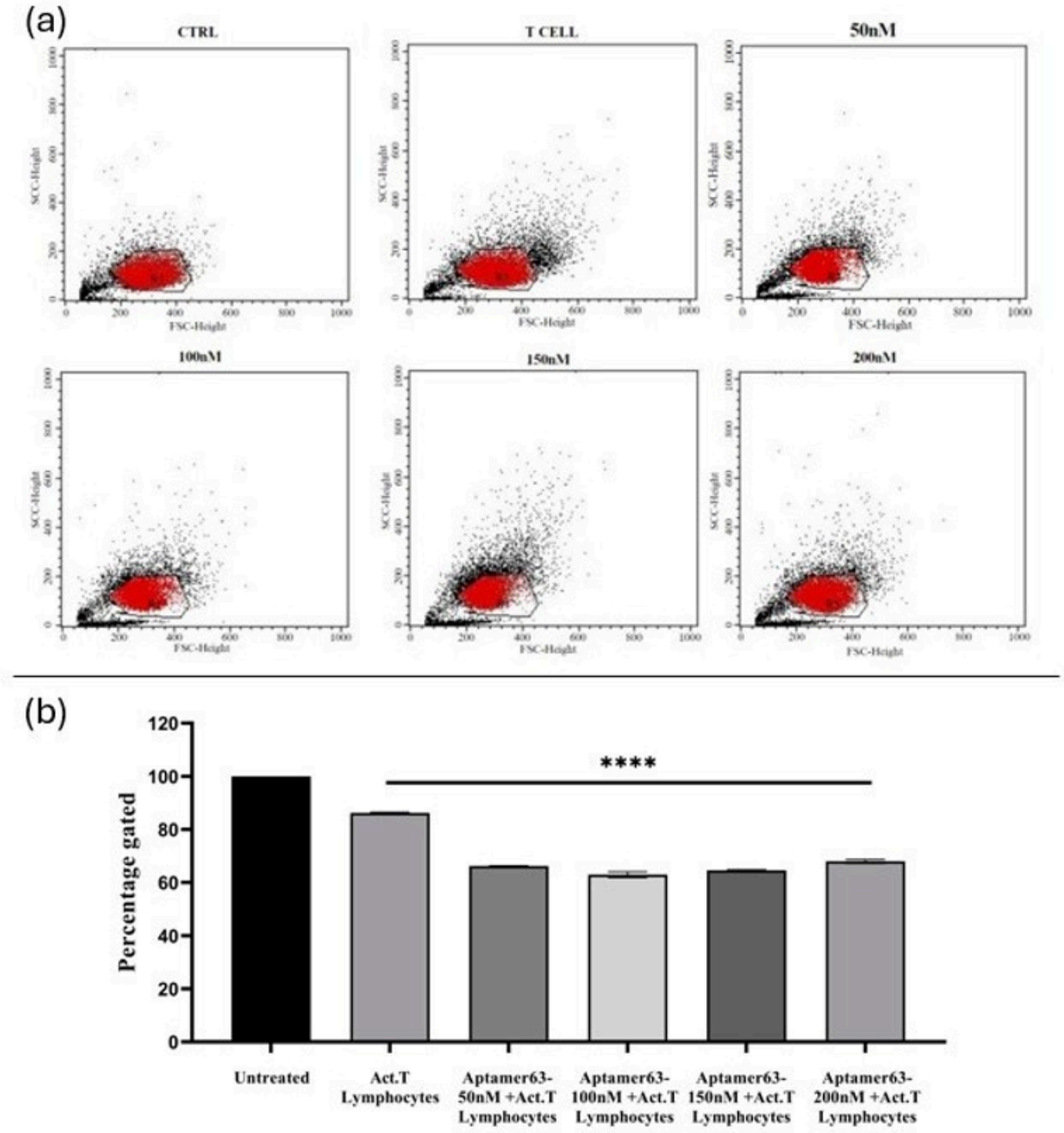

Figure 8

Flow cytometry analysis of aptamer63-mediated cytotoxicity. (a) Flow cytometry dot plots: Representative FSC (forward scatter) versus SSC (side scatter) plots showing cell population distributions for each treatment group. The red oval (R1 gate) encompasses viable cells with intact morphology based on size and granularity. Events outside R1 represent cell debris, apoptotic bodies, and dead cells. Untreated controls and T lymphocyte-treated samples show dense viable cell populations

within R1, while aptamer63 co-treatments (50, 100, 150, 200 nM) show progressively reduced viable populations, with maximum reduction at 100 nM. **(b) Quantification of viable cell populations:** Percentage of cells within the R1 gate for each treatment condition. Untreated controls show ~100% gated cells, T lymphocytes alone reduce viability to ~86%, and aptamer63 co-treatments produce dose-dependent reductions, with 100 nM achieving the lowest percentage (~63%). Data represent mean ± SEM. ****$p < 0.0001$ compared to untreated control.